Investigation of Strain Fields and Anisotropy in Triaxial Tests on Callovo-Oxfordian Claystone by X-ray Micro-tomography and Digital Volume Correlation

H.L. Shi, Thomas Rougelot, S.Y. Xie, J.F. Shao, J. Talandier

▶ **To cite this version:**

H.L. Shi, Thomas Rougelot, S.Y. Xie, J.F. Shao, J. Talandier. Investigation of Strain Fields and Anisotropy in Triaxial Tests on Callovo-Oxfordian Claystone by X-ray Micro-tomography and Digital Volume Correlation. International Journal of Rock Mechanics and Mining Sciences, 2023, 163 (4), pp.105330. 10.1016/j.ijrmms.2023.105330 . hal-04495614

HAL Id: hal-04495614
https://hal.science/hal-04495614v1

Submitted on 8 Mar 2024

HAL is a multi-disciplinary open access archive for the deposit and dissemination of scientific research documents, whether they are published or not. The documents may come from teaching and research institutions in France or abroad, or from public or private research centers.

L'archive ouverte pluridisciplinaire **HAL**, est destinée au dépôt et à la diffusion de documents scientifiques de niveau recherche, publiés ou non, émanant des établissements d'enseignement et de recherche français ou étrangers, des laboratoires publics ou privés.

Investigation of Strain Fields and Anisotropy in Triaxial Tests on Callovo-Oxfordian Claystone by X-ray Micro-tomography and Digital Volume Correlation

H.L. Shi[a], T. Rougelot[a], S.Y. Xie[a], J.F. Shao[a,*], J. Talandier[b]

[a]*Univ. Lille, CNRS, Centrale Lille, UMR9013 - LaMcube - Laboratoire de Mécanique Multiphysique et Multiéchelle, F-59000, Lille, France*
[b]*Andra, 92298 Chatenay Malabry, France*

Abstract

The objective of the present study is to investigate deformation behavior of anisotropic claystone at sample scale in relation with microstructural parameters. For this purpose, a set of five triaxial compression tests are performed on samples of Callovo-Oxfordian (COx) claystone under in-situ X-ray micro-tomography monitoring. Complete 3D images of the samples during whole loading history are recorded and analyzed by digital volume correlation method. Full non-uniform strain fields of samples are determined and averaged global strains are calculated. As novelty, we particularly focus on the effects of bedding planes and confining stress on strain fields. The results indicate that the structural anisotropy of COx claystone has a strong influence on the local strain distribution and cracking process. The confining stress has also an important impact on the strain fields and failure modes of samples in the triaxial tests. The cracking process of samples is strongly correlated with radial strain distribution.

Keywords: Claystone, X-ray micro-tomography, Digital volume correlation, Strain field, Triaxial compression, Anisotropy

1. Introduction

Claystone is considered as potential geological barriers in several countries for underground disposal of radioactive waste (Félix et al., 1996, Birkholzer et al., 2012), due to its low permeability and self-sealing properties (Zhang, 2011, Liu et al., 2016, 2018b). Predictions of mechanical and time-dependent behaviour are essential for the evaluation of underground integrity. For this, it is generally accepted that a multi-scale experimental approach that combines measurement of mechanical properties and time-dependent measurements with micro-structure studies is required to determine the deformation mechanism and develop constitutive equations based on micro-mechanics. A lot of experimental studies, at different scales, have been performed to characterize mineralogy (Robinet, 2008, Robinet et al., 2012, Armand et al., 2014, Robinet et al., 2015), micro-structure (Hicher et al., 1994, David et al., 2007, Laurich et al., 2014, Desbois et al., 2017, Liu et al., 2020) and Thermo-Hydro-Mechanical (THM) properties (Tang et al., 2011, Tsang et al., 2012, Menaceur et al., 2015, Dao et al., 2015, Liu et al., 2018a, Zhang, 2018). It is found that most claystones exhibit a more and less important initial anisotropy, and their THM properties can depend on the loading orientation (Chiarelli et al., 2003, Holt et al., 2011, Ponomaryov and Sychkina, 2015, Liu et al., 2015, McBeck et al., 2018, Zhang et al., 2019, Liu et al., 2019, Grgic et al., 2019, Zeng et al., 2020). For instance, the cracking process induced by mechanical and thermo-mechanical loading is influenced by bedding planes. (Hu et al., 2013, Menaceur et al., 2016, Armand et al., 2017). Standard macroscopic tests only provide global stress-strain responses of sample. The advantage of micro-mechanical tests presented studies is the possibility

*Corresponding author: jian-fu.shao@polytech-lille.fr

to investigate the local strain fields in relations with microstructural parameters such as mineral grains (quartz, calcite, pores).

During the last decades, different kinds of non-destructive techniques, such as BIB-SEM (Broad Ion Beam and Scanning Electron Microscopy), FIB-TEM (Focussed Ion Beam and Transmitted Electron Microscopy) and other means, have been rapidly developed for the characterization of non-uniform deformation and micro-structural evolution (Bésuelle et al., 2006, Buffiere et al., 2010, Houben et al., 2013, Hemes et al., 2015, Robinet et al., 2015, Desbois et al., 2017, Laurich et al., 2018, Cartwright-Taylor et al., 2019, Shi et al., 2020). X-ray micro-tomography has become one of the most widely used non-destructive techniques. The main principles of computerized tomographic imaging can be found in (Kak and Slaney, 2001, Goldman, 2007). This technique has been successfully applied to the deformation and failure analysis of rock-like materials. In recent years, several new test systems have been designed allowing the realization of in-situ tests with X-ray micro-tomographic monitoring (Lenoir et al., 2007, Suuronen et al., 2013, Kaufhold et al., 2016, Yang et al., 2017, Shi et al., 2021b). For in-situ tests of rock-like materials under X-ray monitoring, some researchers have accomplished uniaxial and triaxial experiments. Sun et al. (2017) carried out the real-time uniaxial compression scanning test on cement paste by medical X-ray computed tomography and explored the patterns of porosity evolution during the bearing failure of cement paste backfill. Li et al. (2017) obtained the deformation process of Longmaxi shale under uniaxial compression by X-ray micro-tomography. Birdwell et al. (2013) utilized a uniaxial confinement clamp to investigated fracture development during thermal maturation on Woodford Shale cores by X-ray computed tomography. Recently, Song et al. (2020) explored the anisotropy related to the loading direction of coal, and a series of uniaxial compression tests were

performed. The microstructure and anisotropy were characterized by X-ray micro-tomography. McBeck et al. (2018) and Renard et al. (2019) completed triaxial tests on the Green River shale and sandstone on an X-ray synchrotron platform using the X-Ray-Transparent Triaxial Deformation Apparatus and quantified the 3D strain fields and fracture coalescence with DVC method. Cartwright-Taylor et al. (2020) introduced a network of microcracks into an Ailsa Craig micro-granite sample by heat treatment and investigated the effect of microstructural parameters on the evolution and localization of a random nanoscale crack network by triaxial compression tests on an X-ray synchrotron radiation platform.

High-resolution and high-contrast images obtained from X-ray micro-tomography can be analyzed by different mathematical methods to quantify the full-field and local strains. Various mathematical methods based on Digital Image Correlation (DIC) to solve 2D problems and Digital Volume Correlation (DVC) to solve 3D problems are widely used. The combination of X-ray micro-tomography and DIC/DVC has successfully been used to explore full-field and local displacement and strain in different kinds of materials (Louis et al., 2006, Viggiani et al., 2013, Mao et al., 2019, Lorenzoni et al., 2020). However, only a few studies have so far been devoted to quantitative analysis of full-field and non-uniform local strains as well as cracking processes under complex triaxial compression conditions.

Due to various technical difficulties such as the application of confining stress, triaxial compression tests with X-ray micro-tomography imaging is not easy to perform. In this work, we combine X-ray micro-tomography and DVC to investigate the deformation and failure of the Callovo-Oxfordian (COx) claystone under triaxial compression. The full-field and local strains as well as the development of cracks in the samples were characterized. Five in-situ triaxial compression

tests were performed with X-ray micro-tomography and the acquired images were quantitatively computed by DVC. Finally, the computation results were displayed intuitively through visualization software such as Avizo. Full-field and local strains were discussed, as well as induced cracks. The emphasis was put on the analysis of the anisotropy of the triaxial strain fields, the effects of initial and induced cracks and the failure modes of the samples.

2. Material and methods

2.1. Material characterization and sample preparation

The tested samples of claystone in this study are originally drilled from the COx argillaceous formation of Meuse/Haute-Marne in the underground research laboratory at Bure by the National Agency for the Management of Radioactive Waste (ANDRA). The mineral composition can vary within the stratigraphic levels. In general, the average distribution of minerals in the formation is: 50-55% clay minerals, 20-25% carbonate, ~20% tectosilicates and ~3% heavy metal minerals (*e.g.* pyrite and iron oxide). The clay mineral constitutes a quasi continuous matrix in which the other mineral grains are embedded (Robinet, 2008). The size of these mineral grains is about a few tens of micrometers. The composition of clay minerals is relatively constant: the volume ratio of interstratified illite-smectite, illite and kaolinite-chlorite is approximately 4:2:1 (Armand et al., 2013). However, it is easy to give an accurate estimation on the average size of the various clay aggregates. It is at the scale of a tens of nanometers. It is then not possible to identify such clay mineral particles with the micro-tomography used in this study. Moreover, the inter-particular voids represent the majority of porosity of the clay matrix and the average porosity varies between 14% and 21%. Due to a very small average pore diameter (~ 20 nm), the permeability

of claystone is quite low (10^{-18} to 10^{-20} m^2). The natural water content is between 5% and 8% (Armand et al., 2014, Liu et al., 2016). As a summary, at the mesoscale (scale of calcite and quartz grains), the COx claystone can be seen as a heterogeneous material composed of a clay matrix containing a random distribution of mineral grains. More information on the mineralogy and micro-structure can be found in previous studies (Robinet, 2008, Harrington et al., 2012, Wang et al., 2013, Pardoen et al., 2018). Figure 1 demonstrates the mesostructure of the COx claystone obtained by synchrotron X-ray micro-tomography.

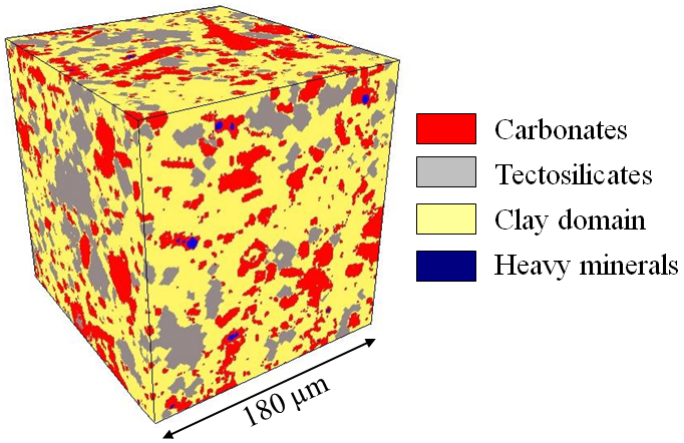

Figure 1: 3D distribution of simplified minerals (Robinet, 2008)

The samples tested in this study are drilled from different orientations with respect to the bedding planes so that we can evaluate the effects of anisotropy on the mechanical properties of the COx claystone. The drilling orientation is defined by the angle θ between the drilling axis and the bedding planes. The five selected values of the angle are θ = 0°, 30°, 45°, 60° and 90° respectively. A total of five samples were deformed in the triaxial compression tests. The core identification and size of samples are given in Table 1. For the sake of convenience, the values of elastic properties and failure stress obtained from the tests presented below are put in the same

table. The tested samples were drilled from three different large cores, which were about 79 mm in diameter and 300 mm in length and conserved in a special container (Conil et al., 2018). Due to the complex preparation procedure and the small size of the samples, the moisture content of the samples was inevitably reduced by approximately 50% (from an average value of 6.9% to about 4.0%). It is important to point out that during the sample preparation and conservation, a number of cracks can be induced in the samples. This phenomenon is amplified when there is an important lose of waste content in the samples.

Table 1: Core identification, size and mechanical properties of five samples with different orientations

Rock core	**Direction**[a]	**Diameter**	**Length**	**Failure stress**	**Axial elastic modulus**	**Poisson's Ratio**
	θ	**(mm)**	**(mm)**	q_{peak}/(MPa)	**E/(GPa)**	ν
EST58125	0°	4.10	7.80	52	9.3	0.21
EST58125	30°	4.20	7.02	21	6.9	0.22
EST58125	45°	3.53	8.48	27	6.6	0.16
EST60710	60°	3.97	7.88	28	7.6	0.23
EST57926	90°	4.10	7.60	44	5.5	0.14

[a] Note: "Direction" is the orientation of the sample's vertical center axis with respect to the bedding planes.

2.2. In-situ triaxial device

A special triaxial compression device (as shown in Figure 2) was used in this research to realize in-situ triaxial compression tests with X-ray micro-tomographic imaging. For the purpose of obtaining high-quality images, the confining pressure cell of the triaxial device is made of a special x-ray transparent polycarbonate with a high tensile and compressive strength. For a sample with a diameter of about 4 mm, a confining pressure of up to 6 MPa and an axial pressure of up to 70 MPa can be applied. As shown in Figure 2(a), the table surfaces in contact with the sample

are also made of the same polycarbonate as the confining cell to reduce contrast at the sample ends in the tomographic images. The device is suitable for oil pressure loading, the axial stress is applied through the indienter and the confining pressure is applied through the base into the cell. In this study, the axial stress and confining pressure were managed by stress-controlled mode with a loading rate of 0.2 MPa/min. All triaxial compression tests were carried out in a conventional room with a constant temperature (19 ± 0.5°C).

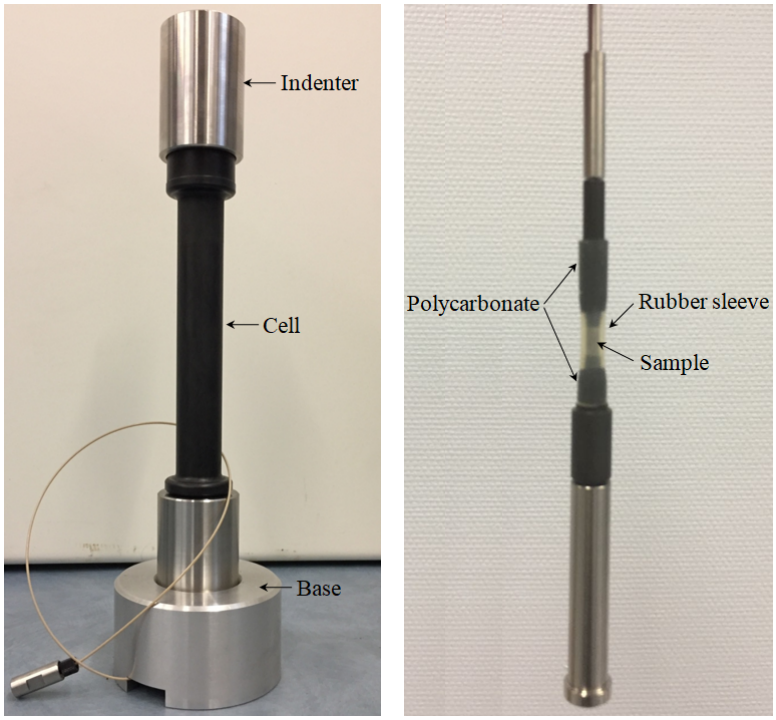

(a) In-situ triaxial test device (b) Sample with rubber sleeve inside the triaxial device

Figure 2: Triaxial test system

2.3. X-ray micro-tomography

X-ray microtomography is a versatile and non-destructive imaging tool, which is increasingly being applied to the meso- and micro-structure research of geotechnical materials. In this study, the

triaxial compression tests were conducted on the In-Situ Innovative Set-ups under X-ray Micro-tomography (ISIS4D) platform (as shown in Figure 3) using a computational tomography system Ultra Tom^R from RX Solutions. In the present study, a 100 kV acceleration voltage is selected with a filament current of 55 μA. Two different voxel sizes of ~5 μm and ~6 μm are obtained respectively for the tested samples ($\theta = 0°$ achieves ~5 μm and others achieve ~6 μm). The samples are irradiated by a beam coming from an X-ray source and rotated a fraction of degree along their vertical axises until a 360° turn. A flat-panel detector (1874×1496 pixels, pixel size 127 μm) has been selected and 1440 radiographs will be taken. The series of acquired 2D radiographs uses a filtered back projection algorithm for 3D reconstruction. Then, the newly 3D images required for the calculation of digital volume correlation can be obtained. Finally, the visualization of 3D images is handled by software such as Avizo and ImageJ.

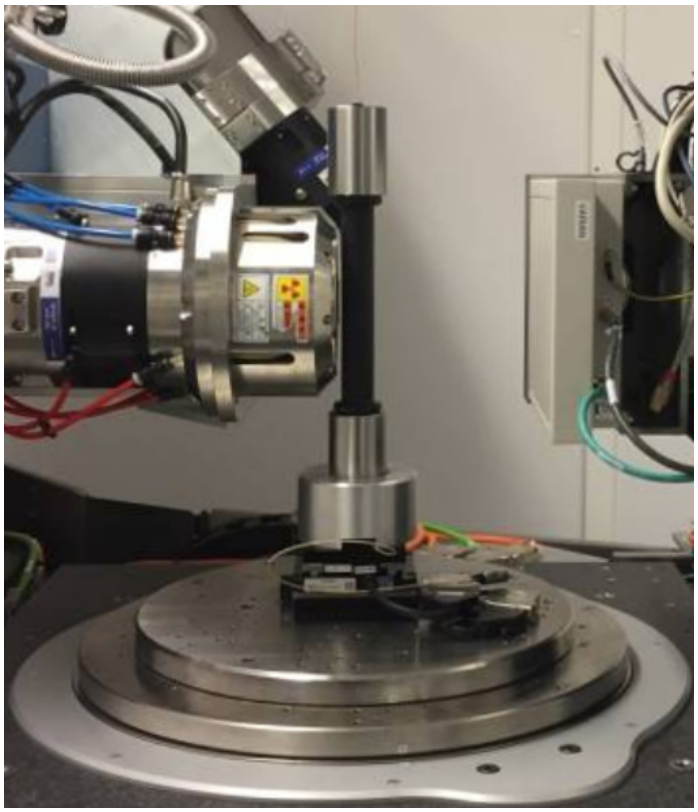

Figure 3: In-situ triaxial compression test of X-ray microtomography

2.4. Digital volume correlation

Digital Volume Correlation (DVC) is a 3D extension of the well-developed Digital Image Correlation (DIC) approach (Chu et al., 1985, Bay et al., 1999). The basic principles of DVC are given in previous research (Kak and Slaney, 2001, Besnard et al., 2006). A DVC platform called YADICs (Seghir et al., 2014), developed in Laboratoire de Mécanique Multiphysique Multiéchelle (LaMcube) was used in the this study. The steps of the DVC process with YADICs are shown in Figure 4. The platform is based on C++, and optimized to process 3D volumes in a reduced time. To identify displacements, several parameters have to be defined: a metric, a sampling, an interpolator, a transformation, an optimizer and finally a regularization method. More details can

be found in (Shi et al., 2020, Shi, 2020).

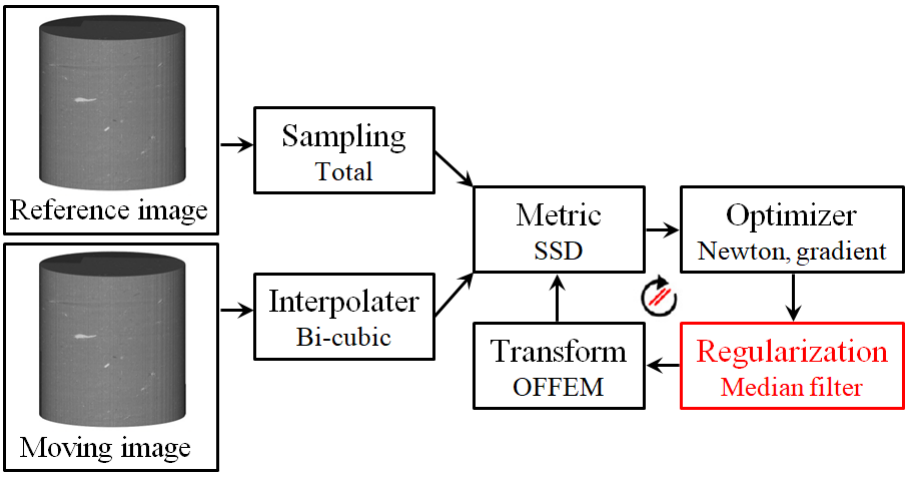

Figure 4: The steps of the DVC process with YADICs

Choosing an appropriate size of element is essential for the calculation of DVC. The results of the local strain calculations show a diffusion phenomenon, *i.e.*, large element size increases the diffusion phenomenon around the local strain concentration zones. Figure 5 illustrates a specific exemplification. Strain fields are calculated by different sizes of elements respectively containing 8, 16, 32 and 64 voxels. The obtained results are strongly sensitive to the element size. In addition, the uncertainty of the displacement field is widely used as a parameter to evaluate the calculation accuracy of DVC. This uncertainty is computed by the standard deviation of the displacement between two images. In this study, a translation of about few microns relative to the reference position was used as the computation of uncertainty. Then, the standard deviation of the displacement field is computed for all the components in three directions. Figure 6 shows the evolution of uncertainty when the element size varies from 4 to 64 voxels. Although the uncertainty of high resolution is higher than that of low resolution, the description of local strain is much better. It is worth noting that all the values of uncertainty obtained here are quite small. Considering the

results of strain localization, the calculated time of DVC and the uncertainty of the displacement fields, the element size with 8 voxels is selected here for the DVC calculation of all triaxial tests. As mentioned previously, the voxel size of the sample with $\theta = 0°$ is ~5 μm and the voxel sizes of the other four samples are about ~6 μm. The pores in the COx claystone are mainly distributed at the nanoscale. The pores in the COx claystone are mainly distributed at the nanoscale (Robinet, 2008). At the micron scale in this study, the pores represent approximately 0.3-0.5% of the total volume of the sample. For hard inclusions, the volume fraction is approximately 0.5% -1.0% (Shi, 2020). However, the hard inclusions are very irregular in shape and widely ranging in size (from a few voxels to several thousand voxels). From a large number of calculations, the results for a DVC window size of 8 voxels have difficulty in reflecting the influence of hard inclusions within 100 voxels on the strain fields.

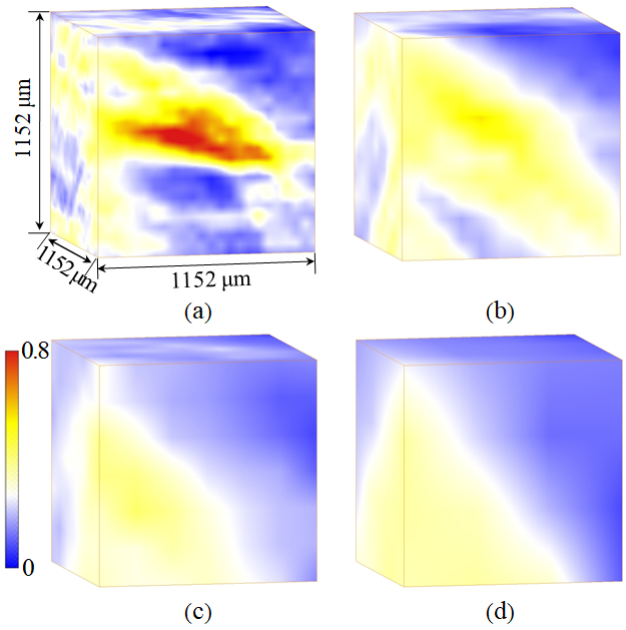

Figure 5: Dependency of calculated axial strain field (%) on element size: (a) 8 voxels, (b) 16 voxels, (c) 32 voxels and (d) 64 voxels

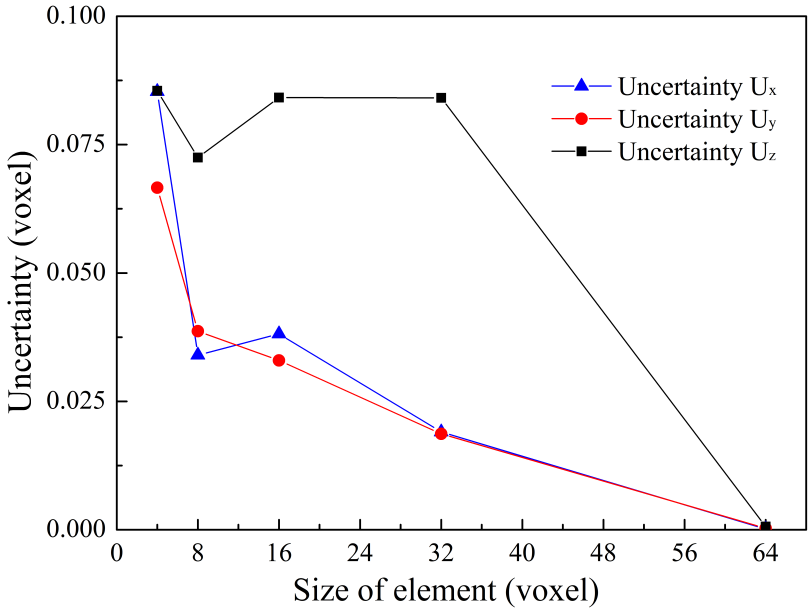

Figure 6: Variations of uncertainty for three components of displacement with different element sizes in DVC calculations in the triaxial test

3. Main results and discussions

3.1. Evolution of average strains

Traditional laboratory testing techniques for measuring deformation such as strain gauges and displacement transducers are not able to provide detailed strain distribution inside samples. Based on highly contrasted 3D tomographic images, DVC technology provides an effective means to quantitatively calculate the local and global displacement and strain fields. McBeck et al. (2018) investigated the deformation processes of micro-strain localization in the Green River shale and the impact of mechanical anisotropy on micro-strain localization using the European Synchrotron Radiation Facility and and DVC.

The global stress-strain relationships of the five claystone samples are shown in Figure 7. It should be noted that points representing the failure strength of each sample were not acquired,

therefore they cannot be present in Figure 7 (except for the sample with $\theta = 30°$). This is explained by the difficulties of the tested sample being scanned at precisely the peak strength. The values of the failure strength for each sample can be found in Table 1. Under the same deviatoric stress, the average radial strains of the tested samples are significantly smaller than the average axial strains. The failure strengths of the three samples with inclined bedding planes ($\theta = 30°$, $45°$ and $60°$) are significantly lower than the other two samples ($\theta = 0°$ and $90°$), (see Table 1). This may be affected by the sliding of the bedding planes as well as the initial cracks in the sample. In addition, the axial elastic modulus of the samples decreases as the θ increases. This indicates that the anisotropy of the samples is affected by the load orientation relative to the bedding planes. This result is consistent with the conclusions of existing macroscopic experiments (Niandou et al., 1997, Zhang et al., 2019). By comparing the results of the tests without confining pressure (see Figure 8) (Shi et al., 2021a), one can see that the failure strengths of the samples ($\theta = 0°$ and $90°$) are significantly enhanced by the applied confining pressure. Furthermore, the confining pressure acts as a strong constraint on the radial strain for samples with inclined angles, *e.g.* samples with $\theta = 45°$ and $60°$.

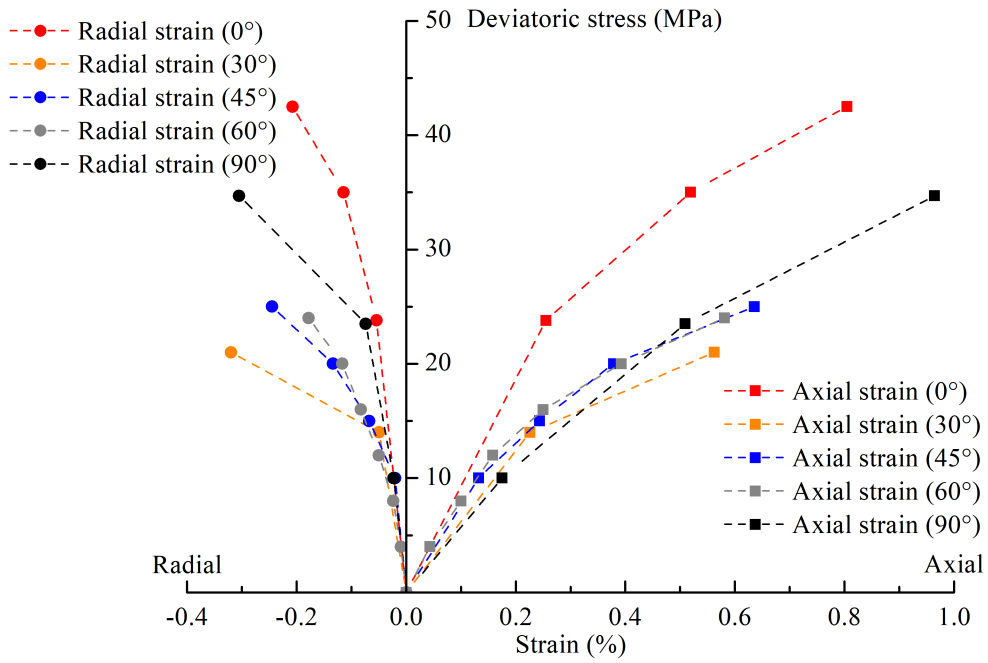

Figure 7: Deviatoric stress versus average radial and axial strains for the five tested samples under a confining pressure of 6 MPa

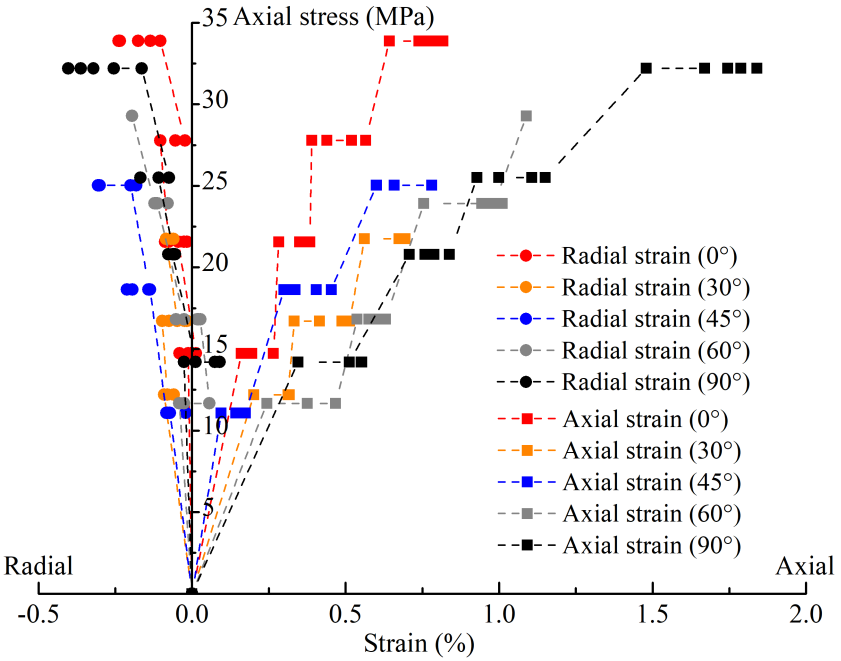

Figure 8: Axial stress versus average radial and axial strains for the five tested samples without confining pressure (Shi et al., 2021a)

Two complete loading-unloading paths are carried out for the samples (θ = 30° and 90°) (as shown in Figure 9). For the sample with θ = 30°, one can see that at about 2/3 of the failure deviatoric stress, the axial elastic strain exceeds 90% of the total axial strain, while the radial elastic strain is only about 30% of the total radial strain. Moreover, the radial non-elastic strain value is significantly larger than that of the axial non-elastic strain. Further viewing the chart of the sample with θ = 90°, one can find that, in contrast to the sample with θ = 30°, the axial non-elastic strain value is several times larger than the radial one. These results reveal that the strain field in the COx claystone is clearly non-uniform and that the deformation of the samples is strongly influenced by the bedding planes. This finding is consistent with the studies by Grgic et al. (2019), Zhang et al. (2019).

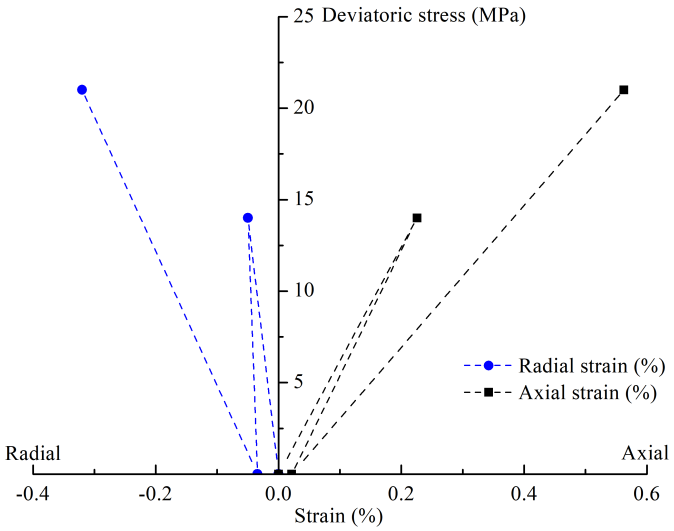

(a) $\theta = 30°$

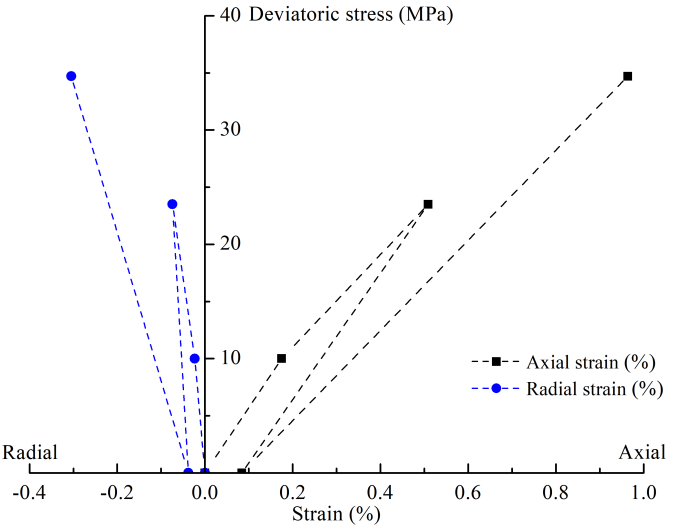

(b) $\theta = 90°$

Figure 9: Deviatoric stress versus average radial and axial strains of the tested samples

At the scale of tested samples, the presence of mineral grains such as quartz and calcite affects the distribution of local strain in the samples. Moreover, during the drilling of cores, preparation and conservation of samples, some cracks can be created in the samples. The existence of suck cracks also affects the local strain field of the samples. Figure 10 shows an example of the sample

with $\theta = 30°$. Benefiting from the comprehensive control of the reconstructed images from samples by DVC technology, the deformation and strain of any selected local zone can be calculated. The effective computational zone of the sample with $\theta = 30°$ is equally divided into two parts (Top and Bottom) along the longitudinal orientation. In Figure 10(a), the initial crack is completely contained within the Top part. The points in Figure 10(b) represent the height of the center position of each part. One can see that the average axial and radial strains (blue color) in the Top part are larger than those in the Bottom part at a medium axial stress. Under peak axial stress, the axial and radial strains (red color) in the Top part are much larger than those in the Bottom part. This difference mainly comes from the crack being compressed and sliding.

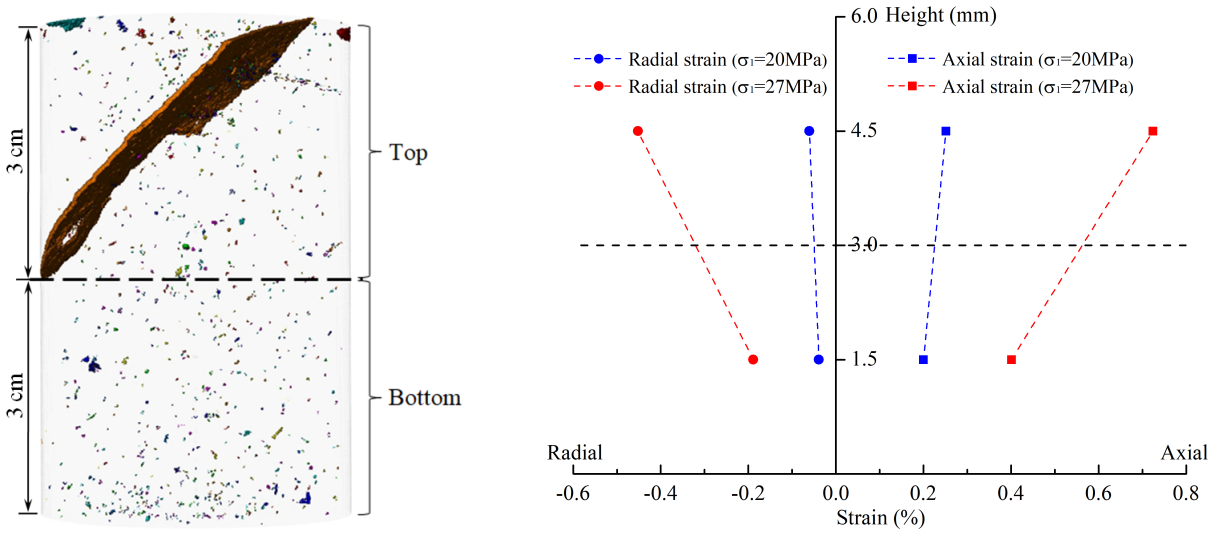

(a) Example of cracks incduced during sample preparation and conservation ($\theta = 30°$)

(b) Average strains of different parts in the sample ($\theta = 30°$)

Figure 10: Average strains of different parts in the sample ($\theta = 30°$)

3.2. Non-uniform full-field strains

As a significant advantage with respect to traditional measurement means, the application of DVC to X-ray micro-tomographic images allows the computation of non-uniform full-field strains

of the sample. Then the full-field strains can be achieved through visualization software such as Avizo. All the axial strain fields and partial radial strain fields (the sample with $\theta = 30°$) of the five samples under different axial stress levels with a confining pressure of 6 MPa are shown in Figure 11 to 15. To facilitate the observation of compression and dilation zones in strain fields, red colour is defined as compression and blue colour as dilation in this manuscript.

From a global perspective, the axial strain fields of the five samples exhibit a strong layered pattern, which is closely related to the orientations of the bedding planes. The layered direction of the axial strain field for the sample with $\theta = 0°$ (see Figure 11) is almost identical to that of the sample with $\theta = 90°$ (see Figure 15). And the layered direction is perpendicular to the direction of the load. This should be caused by the closure of the initial micro-cracks. Moreover, a number of micro-cracks are produced during the processing of the samples. The orientation of those crack is random, but it seems that most cracks are oriented along the bedding planes. The layered phenomenon is obvious and the global axial strain under a given axial stress is larger for the sample with $\theta = 90°$ than that of the sample with $\theta = 0°$. This probably indicates that there is a progressive compaction of weak layers around bedding planes. Additionally, the strain fields present a strong non-symmetry in the vertical direction. This may be caused by the non-uniform distribution of mineral inclusions of the COx claystone or by a test defect (axial stress not being perfectly perpendicular to the end face of the sample). These phenomena above are consistent with the results of the available uniaxial tests (Shi et al., 2021b,a).

The axial and radial strain fields of the sample with $\theta = 30°$ under different axial stresses are shown in Figure 12. As can be seen in Figures 12(a) and 12(d), this sample has a significant initial crack and several new cracks have been generated at peak state. The orientation of the

new cracks is highly consistent with the orientation of the bedding planes (see Figure 18(b)). The same phenomenon was reported in the research performed by Grgic et al. (2019). Under the axial stress of 20 MPa, the initial crack zone exhibits significant compression deformation along the orientation of the axial pressure. At this moment, the initial crack has no significant effect on the distribution of radial strain (see Figure 12(c)). At the peak stress (σ_1 = 27 MPa), one can see particularly large axial strains (>1.5%) around the initial crack and new crack zones. At this point, the influence of the initial crack on the distribution of radial strain can still be considered insignificant. However, the influence of new cracks on the radial strain is remarkable. The radial dilation strain in the entire zone is in excess of 2% (see Figure 12(f)).

In order to better investigate the influence of cracks on local strain, three representative horizontal slices (positions are shown in Figure 16) are selected. The distributions of accumulated axial and radial strains on the selected slices are presented in Figure 17 for the tested sample (θ = 30°) under peak state. An initial crack (thicker) and several new cracks (thinner) can be seen on each selected slice. It can be seen that the axial strains in the initial crack zones of the three slices are very large (red color). For the new cracks that intersect with the initial crack, a relatively large axial local strain can be observed only on slice-850. The local radial strain around the new cracks on the left side of the initial crack is plainly larger than other zones. Interestingly, the local radial strain in the zone where the initial crack and the new cracks overlap is considerable. In addition, the local dilation zone appears next to the largest compression zone in the axial strain field (see Figure 17(h) (dark blue color)). This would be due to the presence of the initial crack causing a strong compression band, which led to a relatively minor tensile zone in the nearby weak zone. Further complicating factors need to be further investigated. Vertical slices of the tested sample

with $\theta = 30°$ under peak stress is displayed in Figure 18. As can be seen in Figure 18(a), the local dilation radial strains (blue) are mainly concentrated around the new cracks zones, and a small amount is distributed in the initial crack zone. Large local compression axial strains (red color in Figure 18(c)) are on the contrary, mainly concentrated in the initial crack zone and a small amount is distributed around the new cracks. The results of this test reveal that tensile cracks in the sample at the peak state are the main reason for the sample failure. Tensile cracks are reflected in the strain fields by dilation in the radial direction and sliding (compression) along the orientation of the maximum principal stress.

The influence of hard inclusions (high-density zones) on the axial strain field is considerable. This influence is related to the size of inclusions. In general, large hard inclusions induce large concentrated local strains (see Figures 13 and 14). However, it is not easy at this stage to provide a quantitative estimation of the critical size of inclusions. These hard inclusions are mainly metal oxides. During the geological deposition process, metal oxide is accompanied by an enormous production of hydrogen, which results to the formation of numerous nano- to micron-scale micro-pores in the clay matrix surrounding the metal oxide zones (Robinet, 2008, Didier et al., 2012). Consequently, strain concentrations are enhanced in these weak porous material zones. This phenomenon was also completely observed in the uniaxial tests (Shi et al., 2021a).

It is worth noticing that in the current study, shear strain fields are not calculated, knowing that those ones could be interesting for the analysis of strain localization in relation with bedding plane orientation. However, in a three-dimensional cylinder sample, it is difficult to calculate shear strains. In our previous study (Shi et al., 2021a), we have considered strain invariants such as von Mises strain. But the conclusion was not really relevant. After comparison, it seems pertinent

to consider axial and radial strains as the main outputs. As presented above, these strains are directly affected by local strain concentration and clearly influenced by bedding plane orientation. Moreover, they can be easily calculated.

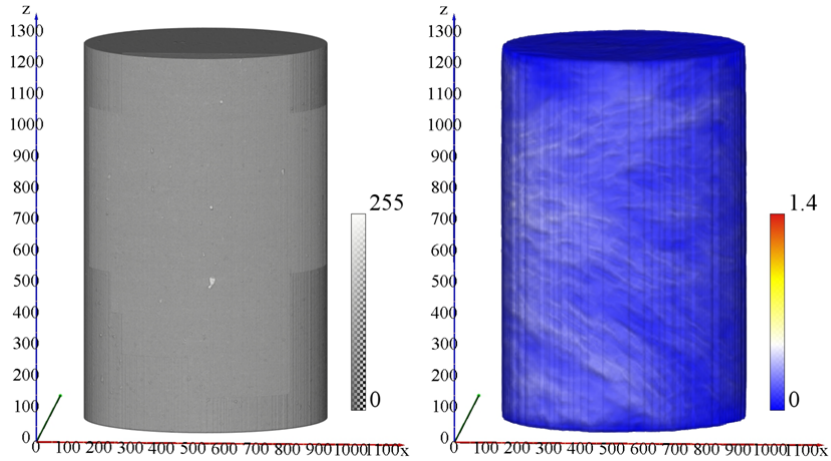

(a) σ_1 = 6 MPa, σ_3 = 6 MPa (b) σ_1 = 29.8 MPa, σ_3 = 6 MPa

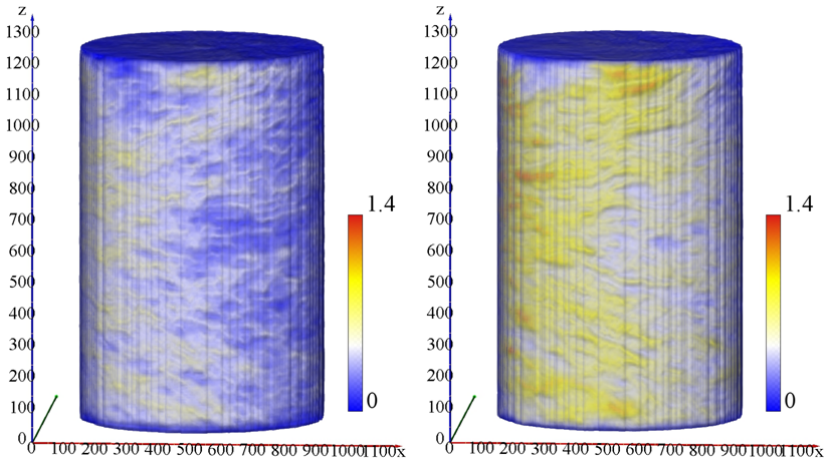

(c) σ_1 = 41 MPa, σ_3 = 6 MPa (d) σ_1 = 48.5 MPa, σ_3 = 6 MPa

Figure 11: Distributions of accumulated axial strain fields (%) in the sample with $\theta = 0°$ under different loads

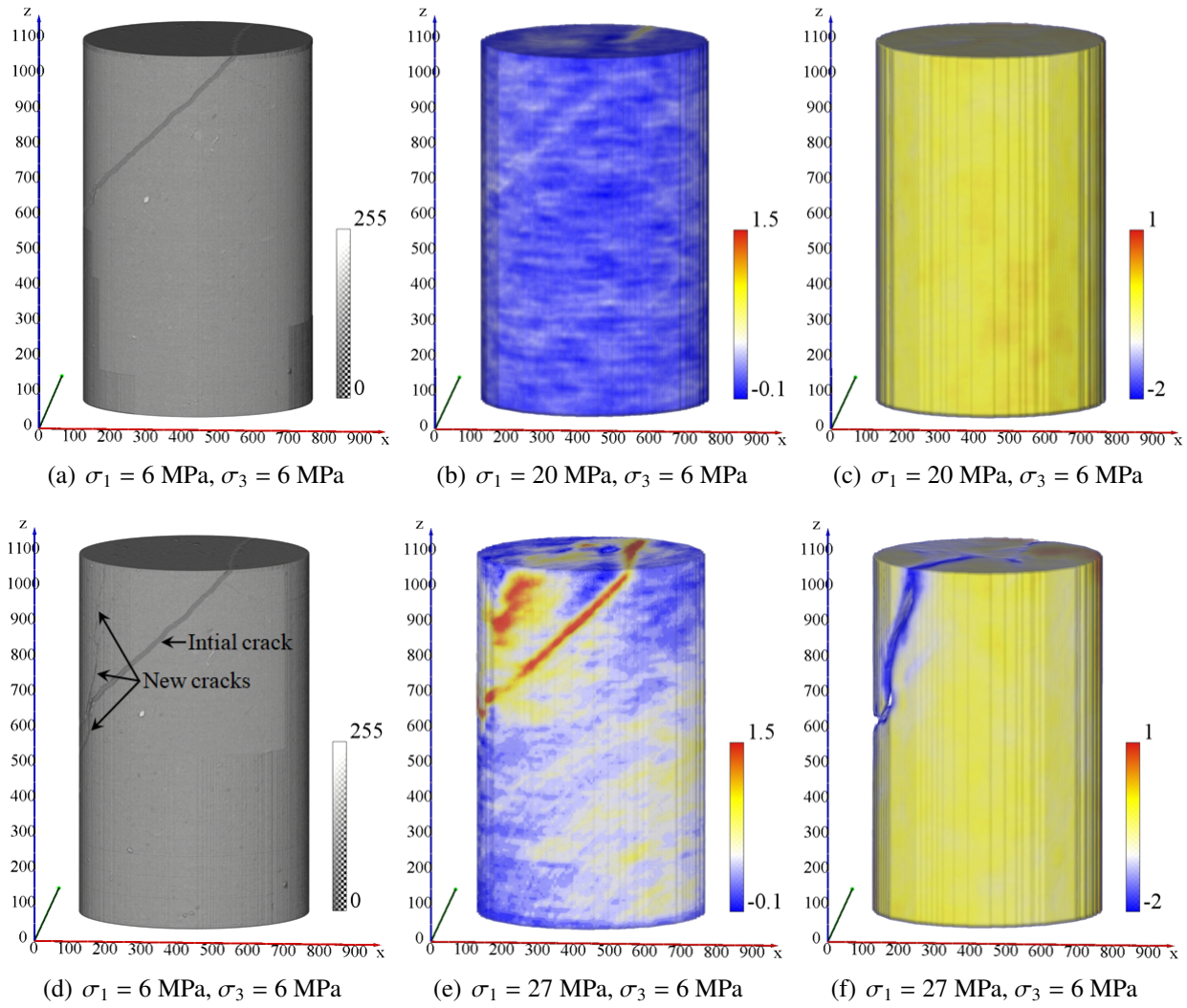

(a) σ_1 = 6 MPa, σ_3 = 6 MPa (b) σ_1 = 20 MPa, σ_3 = 6 MPa (c) σ_1 = 20 MPa, σ_3 = 6 MPa

(d) σ_1 = 6 MPa, σ_3 = 6 MPa (e) σ_1 = 27 MPa, σ_3 = 6 MPa (f) σ_1 = 27 MPa, σ_3 = 6 MPa

Figure 12: Distributions of accumulated axial and radial strain fields (%) in the sample with $\theta = 30°$ under different loads: (a) and (d) are the grayscale maps of the initial and peak states respectively; (b) and (e) are the distributions of axial strains; (c) to (f) are the distributions of radial strains

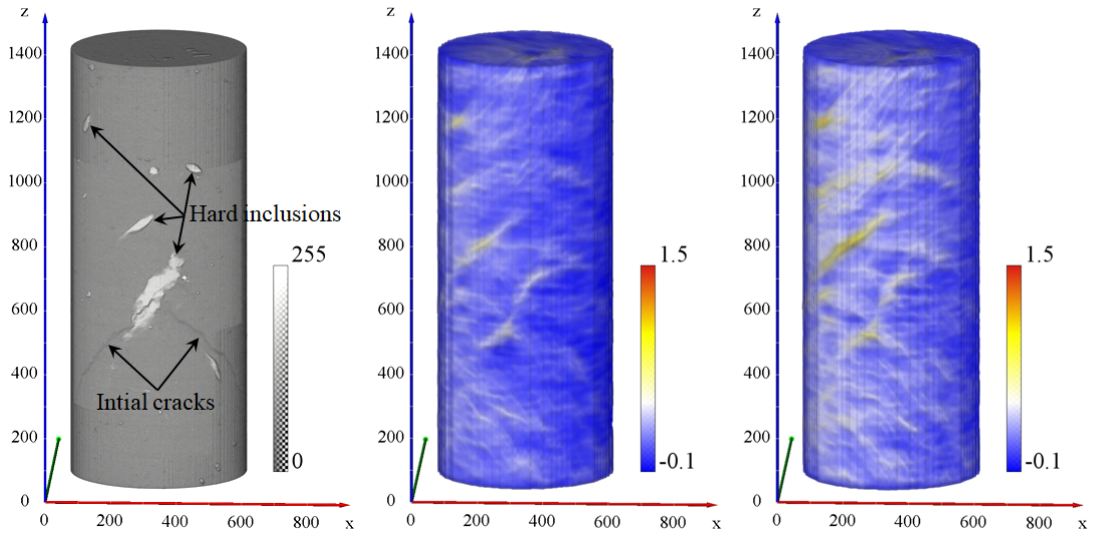

(a) σ_1 = 6 MPa, σ_3 = 6 MPa (b) σ_1 = 16 MPa, σ_3 = 6 MPa (c) σ_1 = 21 MPa, σ_3 = 6 MPa

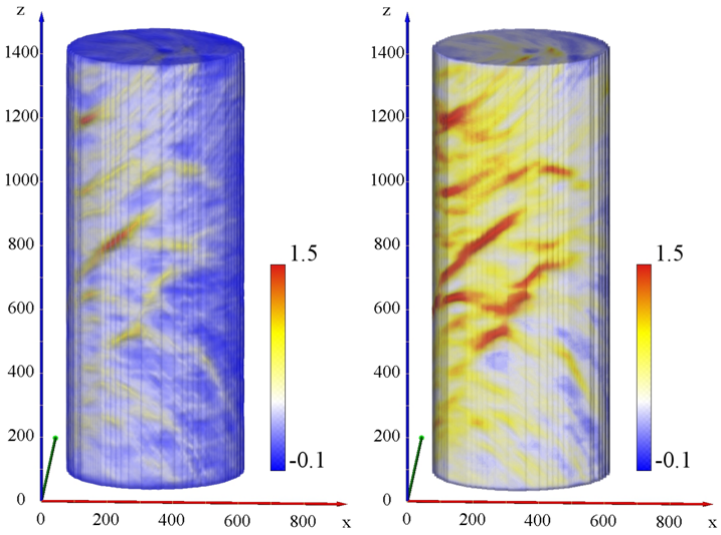

(d) σ_1 = 26 MPa, σ_3 = 6 MPa (e) σ_1 = 31 MPa, σ_3 = 6 MPa

Figure 13: Distributions of accumulated axial strain fields (%) in the sample with $\theta = 45°$ under different loads

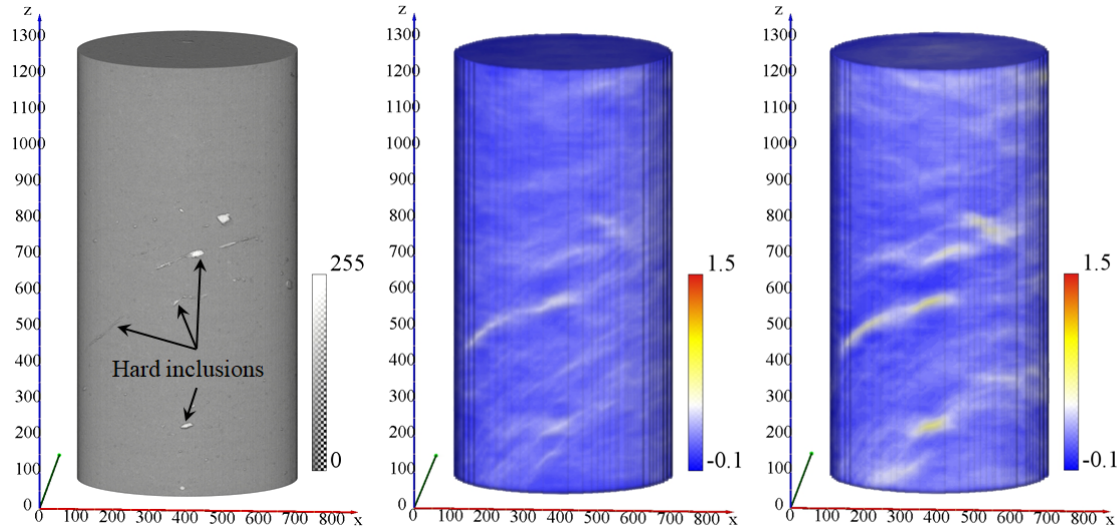

(a) σ_1 = 6 MPa, σ_3 = 6 MPa (b) σ_1 = 14 MPa, σ_3 = 6 MPa (c) σ_1 = 18 MPa, σ_3 = 6 MPa

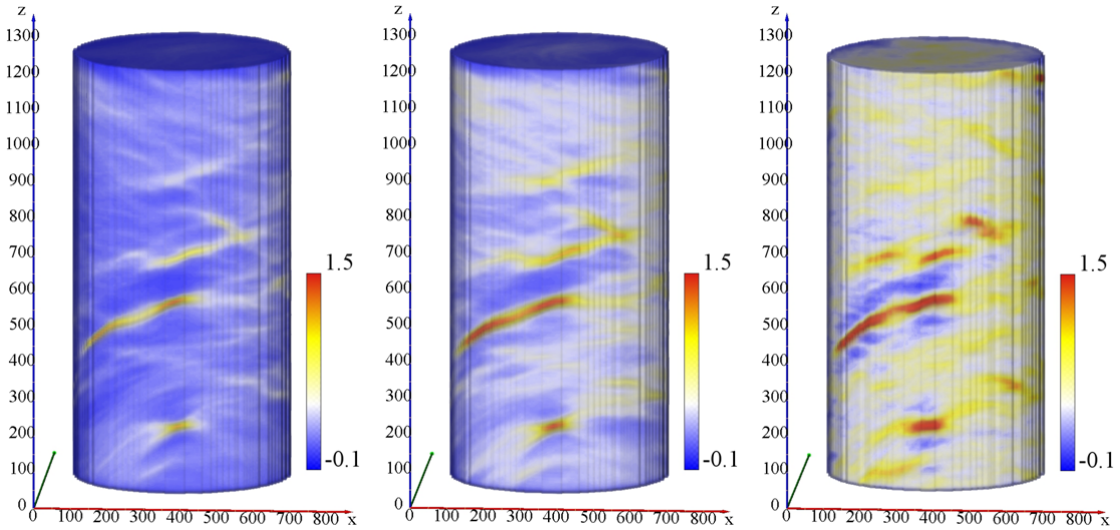

(d) σ_1 = 22 MPa, σ_3 = 6 MPa (e) σ_1 = 26 MPa, σ_3 = 6 MPa (f) σ_1 = 30 MPa, σ_3 = 6 MPa

Figure 14: Distributions of accumulated axial strain fields (%) in the sample with $\theta = 60°$ under different loads

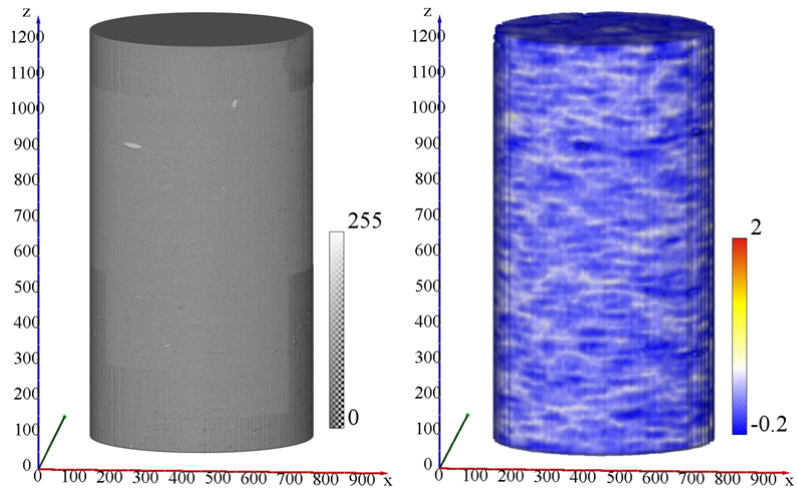

(a) σ_1 = 6 MPa, σ_3 = 6 MPa (b) σ_1 = 16 MPa, σ_3 = 6 MPa

(c) σ_1 = 29.5 MPa, σ_3 = 6 MPa (d) σ_1 = 40.7 MPa, σ_3 = 6 MPa

Figure 15: Distributions of accumulated axial strain fields (%) in the sample with $\theta = 90°$ under different loads

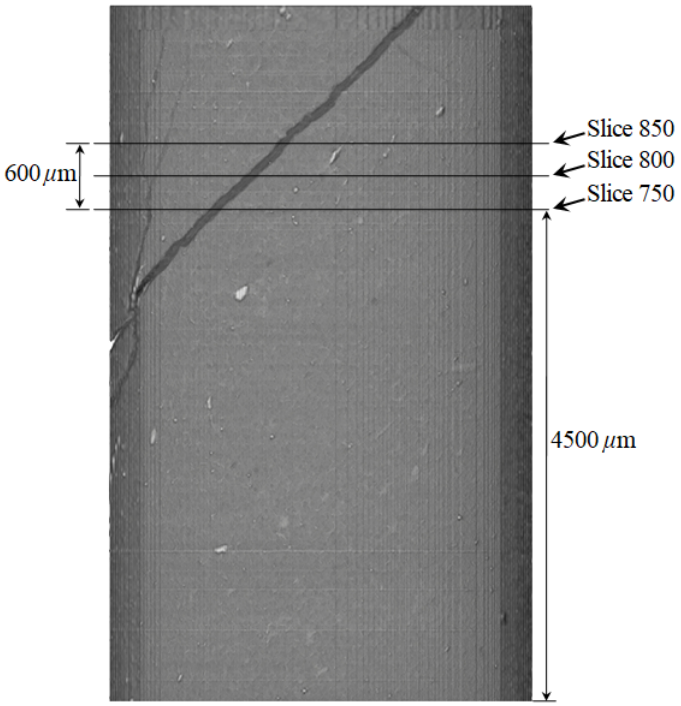

Figure 16: Positions of selected slices in the sample (θ = 30°) for cracking analysis under peak state

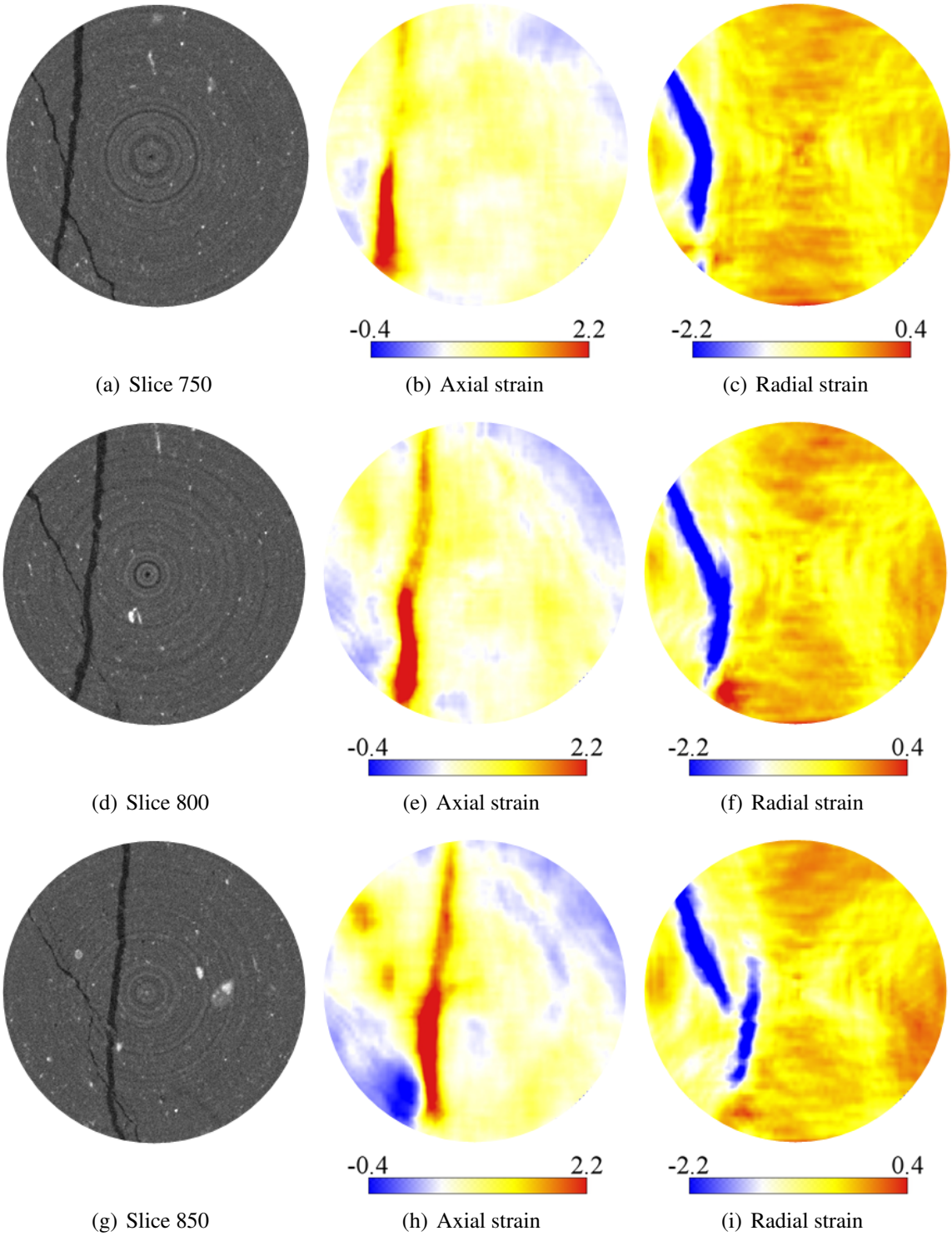

(a) Slice 750 (b) Axial strain (c) Radial strain

(d) Slice 800 (e) Axial strain (f) Radial strain

(g) Slice 850 (h) Axial strain (i) Radial strain

Figure 17: Axial and radial strains (%) distribution maps of horizontal slices at different positions of the sample ($\theta = 30^{\circ}$) under peak state

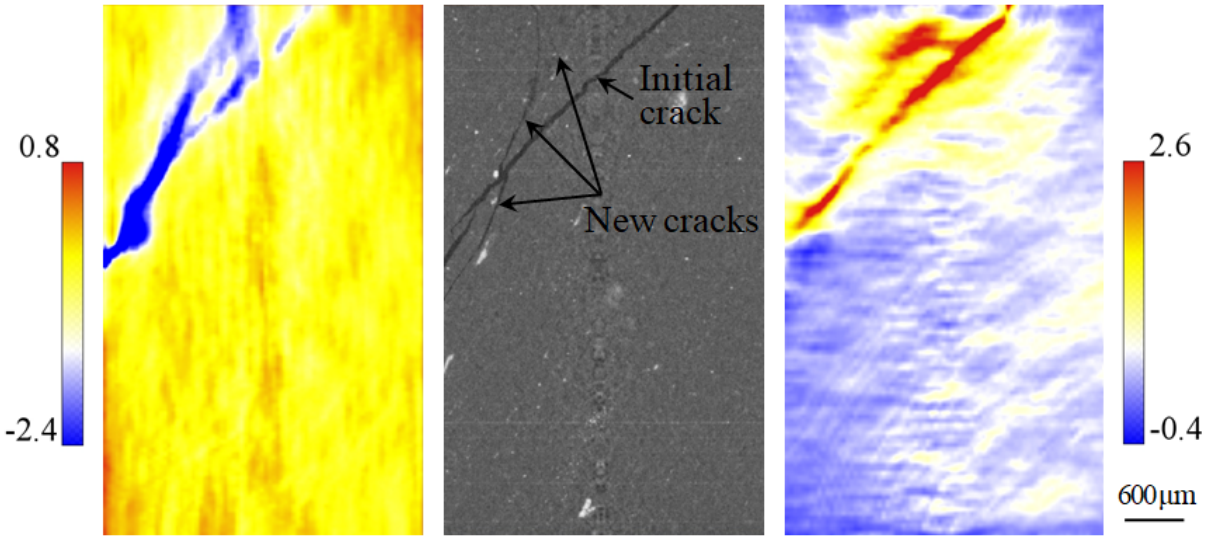

(a) Radial strain (b) Longitudinal slice (c) Axial strain

Figure 18: Axial and radial strains (%) distribution diagrams of a vertical slice through the longitudinal axis of the sample (θ = 30°) under peak state

3.3. Analysis of failure modes

The failure states of the samples after triaxial tests were constructed and are shown in Figure 19. In uniaxial tests, cracking patterns of the COx claystone are clearly influenced by loading orientations with respect to bedding planes (Shi et al., 2021a). Nevertheless, the presence of confining pressure significantly diminishes this effect in the triaxial tests. The major cracks of the samples from θ = 0° to 90° have a similar inclination (yellow lines). These major cracks have angles with respect to the horizontal in a small range between 60° and 66°. The sample with θ = 30° is more complex in the failure mode due to the presence of the initial crack. In terms of fragmentation after sample failure, samples with θ = 30° and 60° were more severely disrupted (The sample with θ = 45° failed to be reconstructed as it was too crushed). This was probably caused by the weak strength of bedding planes. A group of sub-parallel secondary failure cracks

(in the red box) can be seen in Figure 19(c). These cracks would be caused by the opening or sliding of bedding planes in terms of their positions and inclined angles. Similarly, several quasi-horizontal secondary cracks can be seen (in the red box) in Figure 19(d).

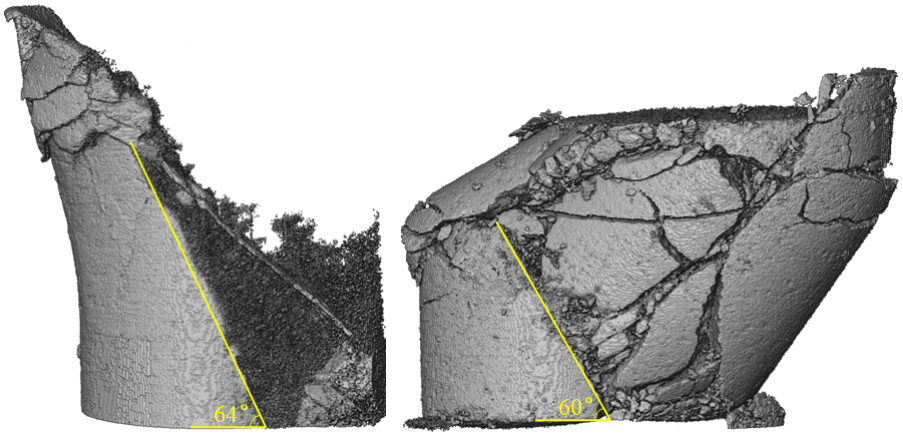

(a) $\theta = 0°$ (b) $\theta = 30°$

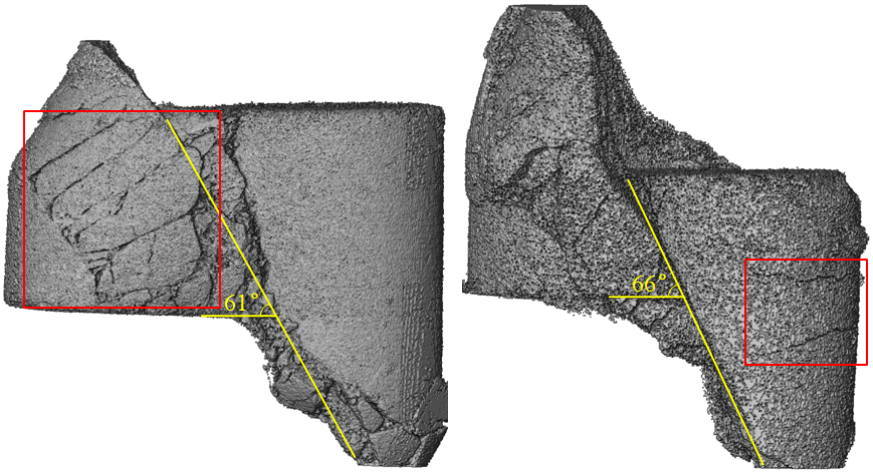

(c) $\theta = 60°$ (d) $\theta = 90°$

Figure 19: 3D reconstruction of tested samples with different loading orientations after failure

4. Conclusions

In this study, in-situ triaxial compression tests have been performed on intact and damaged COx claystone samples using a new triaxial device. X-ray micro-tomography and Digital Volume

Correlation (DVC) were successfully applied to the in-situ triaxial tests on samples of COx claystone. This approach surpasses the traditional measurements and achieves the computation and analysis of full-field and local strains on an anisotropic material under complex stress conditions.

Five samples with different orientations relative to bedding planes were successfully deformed during in-situ triaxial compression tests with a confining pressure of 6 MPa on a X-ray microtomography platform. Both average and local strains of the tested samples are presented. The effects of structural anisotropy have been considered by comparing five different loading orientations.

With the help of the DVC approach, both axial and radial full-field strains of the COx samples are demonstrated. The effects of cracks on local strains have been emphatically analyzed. It is found that the large local strains prefer to produce around the initial cracks and along the loading orientations. Partial results certificate that new cracks are induced by radial dilation deformations. The influences of confining pressure on full-field strains and failure modes have also been analysed. The results indicate that confining pressure reduces the contributions of the bedding planes to the failure modes of the samples. In addition, a strong limitation on radial strain was found in comparison to previous tests without confining pressure.

The DVC results demonstrate that hard inclusions with volumes larger than a certain size will cause localized concentration strains. This should be attributed to the great difference in deformation modulus. However, at this stage, it is not easy to provide a quantitative definition of the critical inclusion size with respect to the sample size. More in-depth studies remain to be accomplished.

COx claystone is an anisotropic material. Local deformations of the samples are clearly in-

fluenced by bedding planes and cracks induced during sample preparation and conservation. This influence comes mainly from the compressed and sliding of bedding planes and cracks. More research on this material under different environmental conditions will continue in future work. Furthermore, only a small number of samples were tested in this work and one single test was conducted for each loading case. Additional studies should be envisaged to investigate the uncertainty of key mechanical properties.

Acknowledgements

The present study was jointly supported by Andra and the ISIS4D X-Ray CT platform. This platform has been funded by the International Campus on Safety and Inter-modality in Transportation (CISIT), the Hauts-de-France Region, the European Community and the National Center for Scientific Research (CNRS). Special thanks are addressed to Jean-Pierre Parent and Jean Secq for their invaluable assistance to the design of experimental device and preparation of samples.

References

Armand, G., Conil, N., Talandier, J., Seyedi, D. M., 2017. Fundamental aspects of the hydromechanical behaviour of callovo-oxfordian claystone: from experimental studies to model calibration and validation. Computers and Geotechnics 85, 277–286.

Armand, G., Leveau, F., Nussbaum, C., de La Vaissiere, R., Noiret, A., Jaeggi, D., Landrein, P., Righini, C., 2014. Geometry and properties of the excavation-induced fractures at the meuse/haute-marne url drifts. Rock Mechanics and Rock Engineering 47 (1), 21–41.

Armand, G., Noiret, A., Zghondi, J., Seyedi, D., 2013. Short- and long-term behaviors of drifts in the callovo-oxfordian claystone at the meuse/haute-marne underground research laboratory. Journal of Rock Mechanics and Geotechnical Engineering 5 (3), 221–230.

Bay, B. K., Smith, T. S., Fyhrie, D. P., Saad, M., 1999. Digital volume correlation: three-dimensional strain mapping using x-ray tomography. Experimental mechanics 39 (3), 217–226.

Besnard, G., Hild, F., Roux, S., 2006. Finite-element displacement fields analysis from digital images: application to portevin-le châtelier bands. Experimental Mechanics 46 (6), 789–803.

Bésuelle, P., Viggiani, G., Lenoir, N., Desrues, J., Bornert, M., 2006. X-ray micro ct for studying strain localization in clay rocks under triaxial compression. Vol. 118. John Wiley & Sons, pp. 35–52.

Birdwell, J. E., Lewan, M. D., Miller, M., 2013. Geochemical changes and fracture development in woodford shale cores following hydrous pyrolysis under uniaxial confinement. In: Unconventional Resources Technology Conference. Society of Exploration Geophysicists, pp. 2012–2019.

Birkholzer, J., Houseworth, J., Tsang, C.-F., 2012. Geologic disposal of high-level radioactive waste: Status, key issues, and trends. Annual Review of Environment and Resources 37, 79–106.

Buffiere, J., Maire, E., Adrien, J., Masse, J., Boller, E., 2010. In situ experiments with x-ray tomography: an attractive tool for experimental mechanics. Experimental mechanics 50 (3), 289–305.

Cartwright-Taylor, A., Butler, I. B., Fusseis, F., Main, I., King, A., Flynn, M., 2019. 4d in-situ x-ray microtomography reveals that material heterogeneity influences microfracture network evolution in deforming rocks. In: Geophysical Research Abstracts. Vol. 21.

Cartwright-Taylor, A., Main, I. G., Butler, I. B., Fusseis, F., Flynn, M., King, A., 2020. Catastrophic failure: How and when? insights from 4-d in situ x-ray microtomography. Journal of Geophysical Research: Solid Earth 125 (8), e2020JB019642.

Chiarelli, A.-S., Shao, J.-F., Hoteit, N., 2003. Modeling of elastoplastic damage behavior of a claystone. International Journal of plasticity 19 (1), 23–45.

Chu, T., Ranson, W., Sutton, M. A., 1985. Applications of digital-image-correlation techniques to experimental mechanics. Experimental mechanics 25 (3), 232–244.

Conil, N., Talandier, J., Djizanne, H., de La Vaissière, R., Righini-Waz, C., Auvray, C., Morlot, C., Armand, G., 2018. How rock samples can be representative of in situ condition: A case study of callovo-oxfordian claystones. Journal of Rock Mechanics and Geotechnical Engineering 10 (4), 613–623.

Dao, L.-Q., Cui, Y.-J., Tang, A.-M., Pereira, J.-M., Li, X.-L., Sillen, X., 2015. Impact of excavation damage on the thermo-hydro-mechanical properties of natural boom clay. Engineering Geology 195, 196–205.

David, C., Robion, P., Menéndez, B., 2007. Anisotropy of elastic, magnetic and microstructural properties of the callovo-oxfordian argillite. Physics and Chemistry of the Earth, Parts A/B/C 32 (1-7), 145–153.

Desbois, G., Höhne, N., Urai, J. L., Bésuelle, P., Viggiani, G., 2017. Deformation in cemented mudrock (callovo-oxfordian clay) by microcracking, granular flow and phyllosilicate plasticity: insights from triaxial deformation, broad ion beam polishing and scanning electron microscopy. Solid Earth 8 (2), 291–305.

Didier, M., Leone, L., Greneche, J.-M., Giffaut, E., Charlet, L., 2012. Adsorption of hydrogen gas and redox processes in clays. Environmental Science & Technology 46 (6), 3574–3579.

Félix, B., Lebon, P., Miguez, R., Plas, F., 1996. A review of the andra's research programmes on the thermo-hydromechanical behavior of clay in connection with the radioactive waste disposal project in deep geological formations. Engineering geology 41 (1-4), 35–50.

Goldman, L. W., 2007. Principles of ct and ct technology. Journal of nuclear medicine technology 35 (3), 115–128.

Grgic, D., Giraud, A., Schoumacker, L., 2019. Dynamic anisotropic elastic properties of a claystone under variable loading direction and saturation. Geophysical Journal International 216 (1), 148–163.

Harrington, J., de La Vaissière, R., Noy, D., Cuss, R., Talandier, J., 2012. Gas flow in callovo-oxfordian claystone (cox): results from laboratory and field-scale measurements. Mineralogical Magazine 76 (8), 3303–3318.

Hemes, S., Desbois, G., Urai, J. L., Schröppel, B., Schwarz, J.-O., 2015. Multi-scale characterization of porosity in boom clay (hades-level, mol, belgium) using a combination of x-ray μ-ct, 2d bib-sem and fib-sem tomography. Microporous and mesoporous materials 208, 1–20.

Hicher, P., Wahyudi, H., Tessier, D., 1994. Microstructural analysis of strain localisation in clay. Computers and Geotechnics 16 (3), 205–222.

Holt, R. M., Bhuiyan, M. H., Kolstø, M. I., Bakk, A., Stenebraten, J. F., Fjær, E., 2011. Stress-induced versus lithological anisotropy in compacted claystones and soft shales. The Leading Edge 30 (3), 312–317.

Houben, M., Desbois, G., Urai, J., 2013. Pore morphology and distribution in the shaly facies of opalinus clay (mont terri, switzerland): Insights from representative 2d bib–sem investigations on mm to nm scale. Applied Clay Sci-

ence 71, 82–97.

Hu, D.-W., Zhang, F., Shao, J.-F., 2013. Experimental study of poromechanical behavior of saturated claystone under triaxial compression. Acta Geotechnica 9 (2), 207–214.

Kak, A. C., Slaney, M., 2001. Principles of computerized tomographic imaging. Vol. Classics in applied mathematics, 33. Society for Industrial and Applied Mathematics, Philadelphia.

Kaufhold, A., Halisch, M., Zacher, G., Kaufhold, S., 2016. X-ray computed tomography investigation of structures in opalinus clay from large-scale to small-scale after mechanical testing. Solid Earth 7 (4), 1171–1183.

Laurich, B., Urai, J. L., Desbois, G., Vollmer, C., Nussbaum, C., 2014. Microstructural evolution of an incipient fault zone in opalinus clay: Insights from an optical and electron microscopic study of ion-beam polished samples from the main fault in the mt-terri underground research laboratory. Journal of Structural Geology 67, 107–128.

Laurich, B., Urai, J. L., Vollmer, C., Nussbaum, C., 2018. Deformation mechanisms and evolution of the microstructure of gouge in the main fault in opalinus clay in the mont terri rock laboratory (ch). Solid Earth 9 (1), 1–24.

Lenoir, N., Bornert, M., Desrues, J., Bésuelle, P., Viggiani, G., 2007. Volumetric digital image correlation applied to x-ray microtomography images from triaxial compression tests on argillaceous rock. Strain 43 (3), 193–205.

Li, X., Duan, Y., Li, S., Zhou, R., 2017. Study on the progressive failure characteristics of longmaxi shale under uniaxial compression conditions by x-ray micro-computed tomography. Energies 10 (3), 303.

Liu, Z., Shao, J., Liu, T., Xie, S., Conil, N., 2016. Gas permeability evolution mechanism during creep of a low permeable claystone. Applied Clay Science 129, 47–53.

Liu, Z., Shao, J., Xie, S., Conil, N., Talandier, J., 2019. Mechanical behavior of claystone in lateral decompression test and thermal effect. Rock Mechanics and Rock Engineering 52 (2), 321–334.

Liu, Z., Shao, J., Xie, S., Conil, N., Zha, W., 2018a. Effects of relative humidity and mineral compositions on creep deformation and failure of a claystone under compression. International Journal of Rock Mechanics and Mining Sciences 103, 68–76.

Liu, Z., Shao, J., Zha, W., Xie, S., Bourbon, X., Camps, G., 2020. Shear strength of interface between high-performance concrete and claystone in the context of a french radioactive waste repository project. Géotechnique, 1–14.

Liu, Z., Xie, S., Shao, J., Conil, N., 2015. Effects of deviatoric stress and structural anisotropy on compressive creep behavior of a clayey rock. Applied Clay Science 114, 491–496.

Liu, Z., Xie, S., Shao, J., Conil, N., 2018b. Multi-step triaxial compressive creep behaviour and induced gas permeability change of clay-rich rock. Géotechnique 68 (4), 281–289.

Lorenzoni, R., Curosu, I., Léonard, F., Paciornik, S., Mechtcherine, V., Silva, F. A., Bruno, G., 2020. Combined mechanical and 3d-microstructural analysis of strain-hardening cement-based composites (shcc) by in-situ x-ray microtomography. Cement and Concrete Research 136, 106139.

Louis, L., Wong, T.-f., Baud, P., Tembe, S., 2006. Imaging strain localization by x-ray computed tomography: discrete compaction bands in diemelstadt sandstone. Journal of Structural Geology 28 (5), 762–775.

Mao, L., Zhu, Y., Wang, Y., Liu, Y., Li, L., Chiang, F.-p., 2019. An improved digital volumetric speckle photography technique with x-ray microtomography and its applications to investigating strain localization in red sandstone. Rock Mechanics and Rock Engineering, 1–10.

McBeck, J., Kobchenko, M., Hall, S. A., Tudisco, E., Cordonnier, B., Meakin, P., Renard, F., 2018. Investigating the onset of strain localization within anisotropic shale using digital volume correlation of time-resolved x-ray microtomography images. Journal of Geophysical Research: Solid Earth 123 (9), 7509–7528.

Menaceur, H., Delage, P., Tang, A.-M., Conil, N., 2015. The thermo-mechanical behaviour of the callovo-oxfordian claystone. International Journal of Rock Mechanics and Mining Sciences 78, 290–303.

Menaceur, H., Delage, P., Tang, A. M., Conil, N., 2016. On the thermo-hydro-mechanical behaviour of a sheared callovo-oxfordian claystone sample with respect to the edz behaviour. Rock Mechanics and Rock Engineering 49 (5), 1875–1888.

Niandou, H., Shao, J., Henry, J., Fourmaintraux, D., 1997. Laboratory investigation of the mechanical behaviour of tournemire shale. International Journal of Rock Mechanics and Mining Sciences 34 (1), 3–16.

Pardoen, B., Dal Pont, S., Desrues, J., Bésuelle, P., Prêt, D., Cosenza, P., 2018. Heterogeneity and variability of clay rock microstructure in a hydro-mechanical double scale fem× fem analysis. In: Micro to MACRO Mathematical Modelling in Soil Mechanics. Springer, pp. 247–256.

Ponomaryov, A., Sychkina, E., 2015. Analysis of strain anisotropy and hydroscopic property of clay and claystone.

Applied Clay Science 114, 161–169.

Renard, F., McBeck, J., Cordonnier, B., Zheng, X., Kandula, N., Sanchez, J. R., Kobchenko, M., Noiriel, C., Zhu, W., Meakin, P., et al., 2019. Dynamic in situ three-dimensional imaging and digital volume correlation analysis to quantify strain localization and fracture coalescence in sandstone. Pure and Applied Geophysics 176 (3), 1083–1115.

Robinet, J., Sardini, P., Siitari-Kauppi, M., Prêt, D., Yven, B., 2015. Upscaling the porosity of the callovo-oxfordian mudstone from the pore scale to the formation scale; insights from the 3h-pmma autoradiography technique and sem-bse imaging. Sedimentary Geology 321, 1–10.

Robinet, J.-C., 2008. Minéralogie, porosité et diffusion des solutés dans l'argilite du callovo-oxfordien de bure (meuse, haute-marne, france) de l'échelle centimétrique à micrométrique. Ph.D. thesis, University of Poitiers.

Robinet, J.-C., Sardini, P., Coelho, D., Parneix, J.-C., Prêt, D., Sammartino, S., Boller, E., Altmann, S., 2012. Effects of mineral distribution at mesoscopic scale on solute diffusion in a clay-rich rock: Example of the callovo-oxfordian mudstone (bure, france). Water Resources Research 48 (5).

Seghir, R., Witz, J. F., Courdert, S., 2014. Yadics-digital image correlation 2/3d software.

Shi, H., 2020. Étude des deformations locales et globales et des processus de fissuration dans l'argilite du callovo-oxfordien par micro-tomographie à rayons x et corrélation volumique. Ph.D. thesis, École Centrale de Lille.

Shi, H., Hosdez, J., Rougelot, T., Xie, S., Shao, J., Talandier, J., 2021a. Influences of structural anisotropy and heterogeneity on three-dimensional strain fields and cracking patterns of a clay-rich rock. Acta Geotechnica 16 (7), 2175–2187.

Shi, H., Hosdez, J., Rougelot, T., Xie, S., Shao, J., Talandier, J., Lacidogna, G., 2020. Digital volume correlation applied to x-ray micro-tomography images in uniaxial creep tests on anisotropic clayey rock. Applied Sciences 10 (14), 4898.

Shi, H.-L., Hosdez, J., Rougelot, T., Xie, S.-Y., Shao, J.-F., Talandier, J., 2021b. Analysis of local creep strain field and cracking process in claystone by x-ray micro-tomography and digital volume correlation. Rock Mechanics and Rock Engineering 54 (4), 1937–1952.

Song, H., Zhao, Y., Elsworth, D., Jiang, Y., Wang, J., 2020. Anisotropy of acoustic emission in coal under the uniaxial

loading condition. Chaos, Solitons & Fractals 130, 109465.

Sun, W., Hou, K., Yang, Z., Wen, Y., 2017. X-ray ct three-dimensional reconstruction and discrete element analysis of the cement paste backfill pore structure under uniaxial compression. Construction and Building Materials 138, 69–78.

Suuronen, J.-P., Kallonen, A., Eik, M., Puttonen, J., Serimaa, R., Herrmann, H., 2013. Analysis of short fibres orientation in steel fibre-reinforced concrete (sfrc) by x-ray tomography. Journal of Materials Science 48 (3), 1358–1367.

Tang, C., Tang, A. M., Cui, Y.-J., Delage, P., Schroeder, C., Shi, B., 2011. A study of the hydro-mechanical behaviour of compacted crushed argillite. Engineering geology 118 (3-4), 93–103.

Tsang, C.-F., Barnichon, J., Birkholzer, J., Li, X. L., Liu, H., Sillen, X., 2012. Coupled thermo-hydro-mechanical processes in the near field of a high-level radioactive waste repository in clay formations. International Journal of Rock Mechanics and Mining Sciences 49, 31–44.

Viggiani, G., Besuelle, P., Desrues, J., 2013. X-ray micro tomography as a tool for studying localized damage/deformation in clay rock. Tech. Rep. 1.

Wang, L., Bornert, M., Chanchole, S., Yang, D., Héripré, E., Tanguy, A., Caldemaison, D., Adams, J., 2013. Microscale experimental investigation of the swelling anisotropy of the callovo-oxfordian argillaceous rock. Clay Minerals 48 (2), 391–402.

Yang, Z., Ren, W., Sharma, R., McDonald, S., Mostafavi, M., Vertyagina, Y., Marrow, T., 2017. In-situ x-ray computed tomography characterisation of 3d fracture evolution and image-based numerical homogenisation of concrete. Cement and Concrete Composites 75, 74–83.

Zeng, Z., Cui, Y.-J., Conil, N., Talandier, J., 2020. Experimental study on the aeolotropic swelling behaviour of compacted bentonite/claystone mixture with axial/radial technological voids. Engineering Geology 278, 105846.

Zhang, C., Armand, G., Conil, N., Laurich, B., 2019. Investigation on anisotropy of mechanical properties of callovo-oxfordian claystone. Engineering geology 251, 128–145.

Zhang, C.-L., 2011. Experimental evidence for self-sealing of fractures in claystone. Physics and Chemistry of the Earth, Parts A/B/C 36 (17-18), 1972–1980.

Zhang, C.-L., 2018. Thermo-hydro-mechanical behavior of clay rock for deep geological disposal of high-level ra-

dioactive waste. Journal of Rock Mechanics and Geotechnical Engineering 10 (5), 992–1008.